HHS Public Access

Author manuscript

Biomaterials. Author manuscript; available in PMC 2019 May 01.

Published in final edited form as:

Biomaterials. 2018 May ; 163: 163–173. doi:10.1016/j.biomaterials.2018.02.014.

Targeting CD14 on blood derived cells improves intracortical microelectrode performance

Hillary W. Bedell[1,2], **John K. Hermann**[1,2], **Madhumitha Ravikumar**[1,2], **Shushen Lin**[1], **Ashley Rein**[1], **Xujia Li**[1], **Emily Molinich**[1], **Patrick D. Smith**[1], **Stephen M. Selkirk**[2], **Robert H. Miller**[3], **Steven Sidik**[4], **Dawn M. Taylor**[1,5], and **Jeffrey R. Capadona**[1,2,*]

[1]Department of Biomedical Engineering, Case Western Reserve University, School of Engineering, 2071 MLK Jr. Drive, Wickenden Bldg, Cleveland OH 44106, USA

[2]Advanced Platform Technology Center, L. Stokes Cleveland VA Medical Center, Rehab. R&D, 10701, East Blvd. Mail Stop 151 AW/APT, Cleveland OH 44106, USA

[3]Neurosciences, The George Washington University, The School of Medicine & Health Sciences, 2300, Eye Street, NW, Ross Hall, Washington DC 20037, USA

[4]Department of Mathematics, Applied Mathematics and Statistics, Case Western Reserve University, 2049 Martin Luther King Jr. Drive, Yost Hall, Cleveland OH 44106, USA

[5]Department of Neurosciences, Cleveland Clinic Lerner Research Institute, 9500 Euclid Avenue, Cleveland OH 44195, USA

Abstract

Intracortical microelectrodes afford researchers an effective tool to precisely monitor neural spiking activity. Additionally, intracortical microelectrodes have the ability to return function to individuals with paralysis as part of a brain computer interface. Unfortunately, the neural signals recorded by these electrodes degrade over time. Many strategies which target the biological and/or materials mediating failure modes of this decline of function are currently under investigation. The goal of this study is to identify a precise cellular target for future intervention to sustain chronic intracortical microelectrode performance. Previous work from our lab has indicated that the Cluster of Differentiation 14/Toll-like receptor pathway (CD14/TLR) is a viable target to improve chronic laminar, silicon intracortical microelectrode recordings. Here, we use a mouse bone marrow chimera model to selectively knockout CD14, an innate immune receptor, from either brain resident microglia or blood-derived macrophages, in order to understand the most effective targets for future therapeutic options. Using single-unit recordings we demonstrate that inhibiting CD14 from the blood-derived macrophages improves recording quality over the 16 week long

[*]Denotes corresponding author Jeffrey R. Capadona, Ph.D. Case Western Reserve University 2071 Martin Luther King Jr. Drive Cleveland, OH, 44107, jrc35@case.edu.

Data availability: The raw data required to reproduce these findings are available to download from http://engineering.case.edu/ebme/Capadona/Research. The processed data required to reproduce these findings are available to download from http://engineering.case.edu/ebme/Capadona/Research.

study. We conclude that targeting CD14 in blood-derived cells should be part of the strategy to improve the performance of intracortical microelectrodes, and that the daunting task of delivering therapeutics across the blood-brain barrier may not be needed to increase intracortical microelectrode performance.

Keywords

intracortical microelectrodes; neuroinflammation; innate immunity; CD14; electrophysiology; gliosis

Introduction

Intracortical microelectrodes (IME) are one of the electrode options for detecting neural signals in cortical neural prostheses and translating them into movement commands to drive an assistive device [1, 2]. IMEs also are a critical research tool for understanding brain circuitry and function. IMEs are the only neural electrode option able to detect single-unit spiking activity from many neurons simultaneously, thus providing higher resolution information compared to other macroelectrode options. However, for research questions requiring long-term chronic recordings and for IMEs to be clinically relevant, they need to function reliably for months to years. Unfortunately IMEs tend to fail over time [3-6]. The cause of IME failure is multi-faceted, and is currently a barrier to successful implementation of this technology [4].

Inflammation plays a central role in the chronic failure of IMEs [4]. This biological response is generated by both the damage associated with insertion of the electrode and the presence of a foreign material in the brain parenchyma [7]. Inflammation resulting from an IME is characterized by immediate damage to the vasculature and subsequent presence of serum proteins and blood in the parenchyma. Soon after, microglia and infiltrating macrophages become activated leading to excessive glial encapsulation, further blood brain barrier (BBB) breakdown, neurodegeneration and neuronal death. This process leads to a reduction of detectable signals necessary for cortical neural prostheses and neuroscience applications [7]. There are many recent studies connecting inflammation to decreased recording quality [5, 8-11]. Saxena *et al.* showed that the integrity of the BBB is directly correlated with microwire IME performance. They concluded that infiltration of myeloid cells following BBB disruption correlates with decreased microwire IME function [8]. Our lab also demonstrated a temporal correlation between the presences of myeloid cell populations (predominantly macrophages) and decreased neuronal density following laminar, silicon IME implantation [12].

Additionally, the inflammation and cellular death that follow implantation of IMEs result in the recognition of “damage” signals, known as damage associated molecular patterns (DAMPS), such as high mobility group box 1 (HMGB1) [13-15]. These DAMPS are recognized by pattern recognition receptors on cells comprising the innate immune response. Cluster of Differentiation 14 (CD14) is a glycosylphosphatidyl-inositol-anchored protein that functions as an innate immune receptor [16]. CD14 is primarily expressed on resident brain microglia and circulating monocytes [17]. CD14 is most notable for its role as the co-

adapter protein for toll-like receptor 2 (TLR-2) and toll-like receptor 4 (TLR-4), TLR-4 being the receptor for lipospolysaccharide (LPS), a component of gram-negative bacteria [18]. In addition to gram-negative bacteria, TLR-4 also recognizes fibrinogen, fibronectin, and other endogenous molecules likely present at the electrode-tissue interface [19-21]. Both TLR-2 and TLR-4 have been shown to recognize necrotic and dying cells [22].

CD14 is also involved in the LPS-independent, TLR recognition of DAMPS [23]. Asea *et al* concluded that CD14 is a co-receptor for heat shock protein 70 (hsp70), a common DAMP released by necrotic cells, leading to the increased production of pro-inflammatory cytokines [23]. A recent study by He *et al.* demonstrated that CD14 plays a fundamental role in the recognition and TNF-α response to S100A9, a DAMP released by neutrophils in inflammation in both mice and humans [24]. Because neutrophils are included in the infiltrating myeloid cells that infiltrate the site of implant, S100A9 is likely present at the electrode-tissue interface [12]. Additionally, CD14 is involved in the recognition of necrotic and apoptotic cells, and subsequent activation of the NF-Kappa B pathway [25, 26]. This pathway is associated with microelectrode implantation in the brain, as many cells are mechanically damaged during the surgical implantation and necrotic cells have been reported around the electrode-tissue interface [6, 14].

Upon activation, CD14-TLR can trigger the release of reactive oxygen species (ROS), and pro-inflammatory cytokines such as TNF-α, MCP-1, Interleukin (IL)-1, -6, -18, through the NF-Kappa B pathway [27-30]. These pro-inflammatory molecules cause further BBB breakdown and neuronal death, perpetuating the inflammatory cascade [14].

Saxena *et al.* demonstrated expression of CD14 around both laminar, silicon and microwire implant interfaces 16 weeks after IME implantation [8]. Additionally, our lab recently concluded that CD14 is a valid therapeutic target to reduce neuroinflammation in response to laminar, silicon IME. In the study by Hermann *et al.,* we explored complete genetic removal of CD14 and the ability of IAXO-101 (Innaxon), a small molecule antagonist to the CD14/TLR4 complex, to improve IME recording performance [10, 11]. Specifically, Hermann *et al.* demonstrated that full removal of CD14 is beneficial to recording performance at acute time ranges, but not necessary in the chronic implantation phase. However, inhibition of the CD14/TLR complex with IAXO-101 exhibited significant improvements in recording performance over the entire 16 week duration without significant differences in endpoint histology. Therefore, we concluded that loss of function on all cell types could prevent normal wound healing, and initiate redundant neurodegenerative inflammatory pathways.

In this study we hypothesized that by selectively targeting CD14, particularly in the infiltrating monocytes, the performance and longevity of IME recordings can be improved by attenuating neuroinflammation and reducing neuronal death around the interface. Given that CD14 is expressed predominantly on both brain microglia and circulating monocytes, we explored the differential role CD14 plays on each of these two cell types by generating and validating chimeric mouse models that knock out CD14 on either microglia (Mg*Cd14*$^{-/-}$) or blood derived monocytes (Bd*Cd14*$^{-/-}$). These two chimeras were compared with wild type and complete CD14 knock outs. Chronic recording performance was investigated over a 16

week time period along with chronic inflammatory events using endpoint histology. Recoding performance was also evaluated in two distinct intervals: the first 12 weeks and weeks 13-16, defined as the chronic modified state (CMS), in order to understand changes in performance based on the epoch event in the progression of neuroinflammation [31]. Decoupling the role CD14 plays in resident brain cells and infiltrating myeloid cells in the neuroinflammatory response to intracortical microelectrodes is critical to developing neuroprotective strategies to facilitate long-term implementation of IME technology.

2. Results

2.1 Neural recording performance

Neural recording was assessed over time using metrics of the total number of recordable units and the percentage of channels on which units can be detected. Here ‘units’ are defined as recordable neurons with action potentials that are separable from the background noise based on distinct wave shapes. Additionally, signal amplitude (max peak-to-peak action potential voltage), and background noise amplitude were calculated along with signal to noise ratio. There is no statistical difference in the signal amplitude, background noise amplitude, or single to noise ratio among all groups. See SI, Results Fig S1, and Fig S2 for supporting data. During the 16-week neural recording experiments, some animals were terminated early due to connector failure unrelated to the brain's neuroinflammatory response. These early terminations account for the decline in number of subjects as the electrophysiology experiment progressed. For consistency immunohistochemical analysis also only included the animals with intact electrode connectors at 16 weeks (see Section 2.2).

2.1.1 Percentage of channels detecting single units and number of single units per channel—The number of single units detected per working channel and percentage of working channels detecting single units are plotted in Fig 1 and Fig 2. The four groups were analyzed for significant differences using a mixed effects linear model to determine if each of the effects (subject, group, epoch, and the interaction between epoch and group) were associated with a statistically higher number of single units detected per channel and/or percentage of channels detecting single units.

Two versions of the mixed effect linear model were generated—one with all four mouse models included in the ‘group’ variable (Fig 1) and one that specifically evaluated the hypothesis that removing BdCd14 would improve recording performance over WT (Fig 2). P-values for both versions of the statistical model are shown in Table 1. Note, ‘subject’ as an effect had an extremely low p-value due to the inherent variability between mice and individual implants. Therefore, ‘subject’ is left off of the tables for simplicity of viewing.

Results in Table 1 indicate a significant benefit in neural recording performance from knocking out CD14 on blood-derived macrophages compared to WT and that relationship likely drove the significant results in the full mixed effect model containing all four mouse types. Fig 2 directly illustrates the significant difference in recording performance between WT and Bd*Cd14*$^{-/-}$ mice.

2.2 Neuroinflammation and neuronal densities at sixteen weeks post implantation

2.2.1 Activated microglia and macrophages—Activated microglia and macrophages were labeled via CD68+ expression. CD68 is expressed in a sub-population of macrophages and microglia that are pro-inflammatory activated [32]. Activated microglia and macrophages are important players in modulating the neuroinflammatory response; activated microglia and macrophages have diverse phenotypes ranging from secreting neurotoxic factors to phagocytosing cellular debris [33]. All experimental groups demonstrated increased CD68+ expression relative to background at the electrode-tissue interface. This expression decayed as a function of distance from the electrode-tissue interface. Inhibiting CD14 (either partial or complete inhibition) had no significant effect on activation of microglia/macrophages around the laminar, silicon IME-tissue interface **(**Fig 3). However, WT animals showed a trend toward increased CD68+ expression between 100 and 250 mm from the interface.

2.2.2. Blood Brain Barrier permeability—The integrity of the BBB is correlated with IME performance [8]. Serum proteins alter the ionic microenvironment of the electrode-tissue interface, potentially creating an unfavorable setting for the recordable neurons [34]. Additionally, the serum proteins also can adsorb onto the electrode surface and increase subsequent inflammatory cell adhesion [35]. Thus, we examined BBB permeability through Immunoglobulin G (IgG) labeling as IgG is one of the three most prevalent serum proteins in the blood. All experimental groups demonstrated increased IgG labeling relative to background at the electrode-tissue interface. IgG expression decayed as a function of distance from the electrode-tissue interface. Expression of IgG was not statistically different between WT, *Cd14*$^{-/-}$, and Mg*Cd14*$^{-/-}$ (Fig 4). However, at a distance of 50-450 μm Bd*Cd14*$^{-/-}$ demonstrated a significantly greater IgG+ expression than WT (Fig 4).

2.2.3 Astroglial encapsulation—Astrocyte encapsulation of the IME in response to the implant results in reduced recording performance through electrical isolation of the IME from the surrounding neurons or the creation of an environment that is not conducive for neurons [36]. Astroglial activation is characterized by increased migration of the cells, hypertrophy, proliferation, and increased expression of glial fibrillary acid protein (GFAP), a component of astrocyte intermediate filament [37]. Thus, we quantified the extent of astroglial encapsulation of the laminar, silicon IME by quantifying GFAP expression as a function of distance from the IME-tissue interface. GFAP expression decayed as a function of distance from the electrode-tissue interface. Contrary to the initial hypothesis, neither partial nor complete inhibition of CD 14 resulted in significantly less astroglial scaring at any distance than WT although complete inhibition showed a trend toward lower expression (Fig 5).

2.2.4 Neuronal density—Neuronal density was evaluated using NeuN+ expression of neuronal nuclei. Having neurons close to the recording contact is important as the recorded amplitude of spikes decreases as a function of distance from the electrode. Although many large neuron types generate spikes that can be detected at distances up to 100 μm or more, most smaller neurons need to be within 50 μm of the electrode to be reliably sorted into single units using available clustering methodology [38]. As expected, neuronal densities

immediately around the electrode were reduced in all mouse models. In spite of the significantly better recording performance of the Bd*Cd14*$^{-/-}$ mice at chronic time points, the neuronal densities of Bd*Cd14*$^{-/-}$ mice were not significantly higher than WT at any distance. These results suggest that the presence of neurons does not guarantee the observed neurons are healthy and firing normally (Fig 6).

3. Discussion

The present study builds from our previous work, by Hermann *et ah,* which outlined the innate immunity receptor CD 14 as a promising target to improve laminar, silicon IME recording quality [10, 11]. Additionally, we furthered our work by considering the role of infiltrating myeloid cells, which have been demonstrated to dominate the neuroinflammatory response to IMEs [12], and mediate IME recording performance [8]. Here, we developed two novel phenotypes of mice to uniquely investigate our hypothesis that the inhibition of CD 14 from only myeloid cells would result in improved neural recording performance in relation to WT animals. We developed mice that either lacked CD 14 in the brain *(*Mg*Cd14*$^{-/-}$*)* or the systemic immune system *(*Bd*Cd14*$^{-/-}$*),* yet retained CD 14 in the opposite. Consequently, animal groups were implanted with functional IMEs for 16 weeks of recording, and underwent post-mortem histological evaluation of neuroinflammation and neurodegeneration.

We assessed recording performance in two discrete time phases: dynamic phase (first 12 weeks) and a steady chronic modified state (CMS) (weeks 13-16). This CMS was first detailed in Prodanov and Delbeke (2016) based on the timing of neuroinflammatory events after IME implantation[31]. Potter *et al.* and McConnell *et al.* have also both independently described a chronic or late stage neurodegenerative state after 12 weeks of laminar, silicon IME implantation [39, 40]. This CMS is defined by persistent factors ever present in the microenvironment of the IME-tissue interface including micromotion, persistent BBB leakage, and production of reactive oxygen species [31]. A mixed effects statistical model that included all four mouse types indicated a significant decline between the initial dynamic phase and the later CMS for both the number of single units detected per channel and the percentage of channels detecting single units from the dynamic phase of inflammation to the CMS, which was expected. Notably the interaction term between phase and group was also significant ($p<0.009$) indicating a significant difference in the decline over time between groups. The most promising scenario would be if knocking out the blood derived CD14 alone would prevent recording decline over time, because long-term neural recording performance could potentially be improved using new therapeutic drugs that do not have to cross the BBB. Our neural recording data support that option as both recording performance metrics were highest over time in the Bd*Cd14*$^{-/-}$ mice. To ensure these improvements over WT mice were significant specifically for the Bd*Cd14*$^{-/-}$ mice, the mixed effect model was run with just the WT and Bd*Cd14*$^{-/-}$ mice as cohorts, confirming a significant difference between groups.

There are many innate immune receptors and signaling downstream to CD14, particularly NF-KB, that can be modified via various upstream events unrelated to CD14 [41]. However, we have recently demonstrated that complete inhibition of CD14 via a knock out mouse

model improves acute stages of laminar, silicon IME recording [11]. Even more notable, we showed that administration of IAXO-101, a small –molecule inhibitor to CD14, resulted in improved neural recordings for laminar, silicon IMEs compared to controls across a 16 week study. Based upon these promising results, we wanted to identify the cell population in which to target CD14. CD14 is expressed in both resident brain cells (microglia) and circulating myeloid cells (macrophages), which inevitably infiltrate the IME implant site. Several studies have suggested that macrophages, not microglia, drive the neuroinflammatory response. For example, in a model of experimental autoimmune encephalomyelitis (EAE), macrophages predominated and correlated with tissue damage and EAE severity [42]. Ravikumar *et al.* has also demonstrated that macrophages were present in a higher density than microglia following laminar, silicon IME implantation in a mouse model [12]. Furthermore, blood derived macrophages are more phagocytic and inflammatory compared to those cells of a microglial lineage [43]. Moreover, since IAXO was delivered subcutaneously, the small molecule inhibitor is much more likely to target CD14 in myeloid cells than brain resident microglia.

Thus, the current study also corroborates the recent results of Hermann *et al.*, in which IAXO-101, most likely targeted CD14 in the myeloid cells, not the resident brain cells. However, it is important to note that the bio-distribution of IAXO-101 following microelectrode implantation has not been reported. Again, delineating the function of microglia and macrophages, and elucidating their roles in the innate immunity pathways is a prerequisite to developing therapeutic interventions to decrease inflammation caused by penetrating injuries to the brain, as an IME implantation. Therefore, our results suggest that systemic administration of therapeutic targets to inhibit CD14 from infiltrating myeloid cells may be sufficient to improve IME recording, relieving therapeutic approaches from the daunting task of crossing the BBB.

Interestingly, recording improvements seen in the complete CD14 knock out were not as strong as when CD14 was only inhibited in the macrophages. Conceivably, some CD14 signaling in the microglia is beneficial to maintain an environment more hospitable to normal neuronal function. Although both microglia and macrophages participate in the neuroinflammatory response to IME implantation, there are small, but perhaps noteworthy, differences in their roles. For instance, microglia, not macrophages, communicate with the neighboring neurons in their ramified state [44]. It is possible that CD14 signaling enables the microglia to elicit a more neuroprotective effect during inflammation, than in the absence of CD14 signaling.

It is important to note that this type of study inherently results in a great deal of mouse-to-mouse variation in recording performance. Thus, the mixed-linear effects model indicated that individual mouse was a highly significant ($p < 0.001$) predictor for recording quality. This is not a unique result as other groups have demonstrated noteworthy differences in recording performance and end point histology despite using the same type of microelectrode and following a heavily controlled implantation procedure [9]. As previously reported by the Otto group [45], we identified major differences in histology along the depth of the electrode, prompting our lab to take an average of 4-6 slices per animal at evenly spaced intervals along the IME for histological analysis.

One of the hypothesized factors accounting for both recording and histological variability across animals is distance of implantation site to major vasculature. Even under the most controlled surgical implantation of the electrode, it is very difficult to choose an implant site which avoids penetration through major vessels [46]. Implanting the electrode through a major vessel results in increased bleeding and blood infiltration into the parenchyma which has been shown to reduce recording quality [8, 46]. During all surgical implantations, bleeding levels were tabulated, and it was very rare excessive bleeding was visualized either during drilling or insertion of the IME. Most of the time, there is little to no surface bleeding. However, using 2-photon microscopy Kozai *et al.* reported that visualized surface bleeding is not a reliable metric for overall bleeding within the cortex caused by implantation [46]. The randomness of the proximity of a major blood vessel to the implantation site likely contributed to the high level of variability we saw between animals even from the same group. Additionally, mouse to mouse variability, differences in surgical induced bleeding, and subtle differences in experimental design and set up could account for differences in the effectiveness in complete inhibition of CD14 in acute recording performance between our prior study and the current study.

The observed decrease in recording quality over time for all groups coincided with neuroinflammation and neuronal dieback around the electrode shown by IHC analysis (Fig 6). This decline in recording quality and loss of neurons has been described by many groups [3, 5, 40, 47]. A few studies have attempted to correlate end point histology and IME recording quality. The Meng and Pikov labs jointly identified positive correlations between recording quality (percentage of active sites and average SNR) and histological markers of neuronal density. Meng and Pikov also found negative correlations between the respective recording metrics and glial markers at the electrode-tissue interface of a Parylene C probe doped with neurotrophic and anti-inflammatory factors [48]. Three years later, Pikov collaborated with the Cogan lab to identify positive correlations between histological markers (chronic neuronal density and glial markers) and early action potential amplitude of chronically implanted ‘Utah’-type IMEs [49].

In this present study, inhibiting CD14 in just the myeloid cells (Bd*Cd14*$^{-/-}$) improved recording performance over wild type but did not mitigate the inflammatory response at 16 weeks post implantation relative to the control. Furthermore, in contrast to a study by Saxena *et al.* that demonstrated a correlation between recording performance of microwires and BBB breakdown, we saw more BBB breakdown in Bd*Cd14*$^{-/-}$ mice that had the better recording performance over the course of the study (Fig 2, Fig 5) [8]. Unlike the Saxena study, in this present study, the macrophages allowed in by BBB breakdown were CD14 negative, which likely mitigated some of the complications normally associated with infiltrating macrophages. It is important to note that the Saxena study examined the relationship between BBB breakdown and the recording performance of microwires, not laminar, silicon IMEs as in this study. In addition, Saxena *et al.* also found that laminar, silicon IMEs result in greater chronic BBB breach compared to microwires. Furthermore, microwires historically yield greater recording quality compared to laminar, silicon IME [6].

Histology presents just a snapshot in time of the inflammatory response and neuronal density. The inflammatory response is dynamic. Thus changes along the course of the study

can affect neuronal health and activity as well as the microenvironment of the electrode-tissue interface [39]. To that end, Kozai and Cui have suggested that endpoint histology is not always correlated to recording quality [9]. Additional factors that may contribute to the discrepancy between our histology and recording results include the fact that the simple presence of neurons near the electrode does not guarantee those neurons are healthy and firing. Furthermore, cellular production of reactive oxygen species can cause electrode materials breakdown and delamination of the insulation and conductive traces resulting in the loss of recording ability even if healthy neurons are still within a recordable distance [50, 51]. SEM images were taken of representative explanted probes and pre-implanted probes for comparison. Figure 7 shows images of pre-implanted and explanted probes. Explanted probe shown was from an animal which yielded poor recording over 16 weeks. No observed defects were seen in this electrode suggesting that the integrity of the materials composing the implants had little effect on the recording quality.

In future work, strategies addressing the biological response to these electrodes need to be coupled with strategies to mitigate mechanical failure modes. Additional studies are underway by our lab targeting CD14 along with complementary materials that attempt to combat/counter act the mechanical mismatch between the brain parenchyma and stiff electrode. This mismatch evokes strain on the tissue thus further propagating the inflammatory response [52]. We hope to determine whether the promising effects resulting from both approaches are additive or even synergistic in mitigating neuroinflammation to IMEs. While many studies in the field focus on targeting a single aspect of the complex problem, we believe more work needs to be done to look at the complementary effects of various approaches to improve the function and stability of intracortical microelectrodes. The data presented here suggests targeting CD14 pathways on infiltrating macrophages may be a practical compliment to any comprehensive strategy to develop electrodes that can record for a lifetime.

4. Conclusion

Using novel chimeras, we demonstrated that inhibiting CD14 in just myeloid cells can improve intracortical microelectrode performance in both the percentage of channels able to detect one or more neurons and in the number of units detected per working channel over a 16 week timespan. Results from these unique chimera models are important because they demonstrate that targeting CD14 in just the myeloid cells can be a promising approach to achieve long-term functionality of intracortical microelectrodes, without broad immunosuppression that could be deleterious to patients, or requiring complicated approaches to deliver therapies across the BBB. Further, combining specific cellular targets like CD14 with other engineering strategies to improve IME function should be explored to extend the lifetime of intracortical microelectrodes for neuroscience research and clinical brain computer interfacing applications.

5. Methods

5.1 Animals

C57/BL6 (strain #000664) and *Cd14*$^{-/-}$ (C57/BL6 background, strain #003726) mice were obtained from Jackson Laboratory and bred in-house. Genotyping was performed to verify strain of all mice used in this study prior to surgery according to the protocols established by the vendor (Jackson Laboratories, SI, Methods, 2.1). Both male and female mice were used as all mice that were bred were used and not biased based on sex. When we group mice that undergo the same electrophysiology procedure in this paper, we found that over the course of a 16 week trial, only one time point (at 6 weeks) demonstrated a significant difference between control animals (Fig 8). It is currently unclear why 6 weeks post-implantation yields a significant difference in recording performance between male and female mice. Additionally, we performed a power analysis on the data set in Fig 8 to determine the number of animals needed to identify difference by sex. Aside from the one time point that has already shown significance, additional time points would require as many as 5500 mice in each group, and an average of 686 mice per group (data not shown). Therefore, based on the lack of difference in the recording quality of control electrodes implanted in males versus female mice, we did not bias animals used based on sex. The final sex composition of groups was mixed but yielded at least double the number of males as females for all groups: BdCd14$^{-/-}$: 3 female, 8 male; MgCd14$^{-/-}$: 3 female, 9 male; Cd14$^{-/-}$: 3 female, 7 male; wildtype: 3 female, 6 male.

Mice, were between 6-10 weeks of age at the time of all procedures. Chimeras were created when mice were 6-8 weeks of age and microelectrode implantations were conducted when mice were 8-10 weeks of age. Note, BdCd14$^{-/-}$ N= 8-11; MgCd14$^{-/-}$ N= 9-12; Cd14$^{-/-}$ N=8-10; wildtype N=6-9. The number of animals in each experimental group are provided as a range. The larger number of the range is the number of animals per condition that underwent surgery; the smaller number of the range is the minimum number of animals of that condition for any data point.

Prior to implantation surgery, animals were housed in groups (3-5 per cage) with food and water while maintained on a 12-hour light/dark cycle. All animal practices were performed in a class II sterile hood using microisolator techniques. All procedures and animal care practices were approved by and comply with the Case Western Reserve University Institutional Animal Care and Use Committee.

5.2 Genotyping

Tail snips were collected at approximately ten days of age and digested overnight at 55°C in Direct PCR Lysis buffer (Viagen) and Proteinase K (Viagen). PCR was run on mouse tail DNA samples using the following primers: **CCG CTT CCA TTG CTC AGC GG** (Mutant forward), **CCA AGT TTT AGC GCT GCG TAA C** (Wild type forward), **GCC AGC CAA GGA TAC ATA GCC** (Common reverse). Following PCR, bands were separated by gel electrophoresis on a 1.5% agarose gel. Homozygous mutant (*Cd14*$^{-/-}$) mice are expected to have a band at ~600 bp. Homozygous wild-type (WT, *Cd14*$^{+/+}$) mice are expected to have a band at ~840 bp PCR analysis confirmed genotype of all mice used in this study.

5.3 Creation and validations of bone marrow chimeras

To investigate the effects of selectively targeting CD14 on either circulating monocytes or resident brain microglia a bone marrow chimera mouse model was utilized. Chimera mice were created using previously described methodology [12, 43]. Irradiated wildtype (WT) mice received bone marrow (BM) from *Cd14*$^{-/-}$ mice creating chimeras where the CD14 gene was selectively knocked out from only the blood derived cells (Bd*Cd14*$^{-/-}$) (Fig S3A). Irradiated *Cd14*$^{-/-}$ mice received WT BM to create chimeras allowing the CD14 gene to be selectively inhibited from only the resident brain microglia (Mg*Cd14*$^{-/-}$, Fig S3B). C57/BL6 or *Cd14*$^{-/-}$ mice were irradiated at 4-8 weeks of age with 1000 rads of Cs^{136} gamma radiation. Within 4-6 hours following irradiation, bone marrow (BM) cells were isolated from the femur on non-irradiated mice of the other genotype and transplanted via tail vein injection into the irradiated mice (200 μL, 25-35 million cells/mL). After irradiation, eliminated monocytes are replaced by BM donor cells. Chimeric mice were given acidic water (pH 3.0) and allowed to recover at least 14 days after the BM transplant. Additionally, one mouse within each group of irradiated mice did not receive the BM cells to verify that bone transplant success was necessary for survival of the animal. The animal from each group who did not receive the BM transplant did not survive past 12 days. Transplant effectiveness was further confirmed by Complete Blood Count (CBC) analysis and fluorescence-activated cell sorting (FACS) analysis using protocols described previously [12]. Prior to IME implantation, transplant efficiency of chimeras (Bd*Cd14*$^{-/-}$ and Mg*Cd14*$^{-/-}$) was measured using complete blood count (CBC) analysis and fluorescence activated cell sorting (FACS) analysis. CBC analysis was performed comparing cell populations in whole blood between each chimera and non-irradiated WT and *Cdl4*$^{-/-}$ controls. Cell populations were within normal limits for all mice (Table SI). Further, CBC analysis of blood samples showed no significant difference between each chimera and non-irradiated WT and *Cdl4*$^{-/-}$ controls. Additionally, FACS analysis was used to confirm the presence or absence of circulating CD14+ cells in the blood for each chimera animal. FACS analysis demonstrated that CD14+ cells were detected in the blood for Mg*Cd14*$^{-/-}$ chimera mice (5.3 ± 1.20%), and was not significantly different from the WT population (6.21 ± 1.49%). Additionally, CD14 was detected in very low quantities in both Bd*Cd14*$^{-/-}$ chimera mice (1.03 ±0.52%) and *Cdl4* mice (1.15 ± 0.67%) indicating low background autofluorescence of CD 14+ reactivity in blood non-specific binding of the antibody in blood samples. Collectively, our data confirms successful bone marrow transplant of both chimeras.

5.4 Electrode pretreatment

Prior to surgery, 1 kHz impedance measurements were measured in saline to confirm the impedance magnitude for all channels matched values provided by the vendor. After rinsing any residual salts off in deionized water, all probes were sterilized via a hot ethylene oxide gas cycle.

5.5 Surgical details

Single shank, 16 channel Michigan style electrodes with iridium contact sites (A16-3mm-100-50-177-Z16) (NeuroNexus) were implanted into the primary motor cortex.

See SI, Methods, 2.4 for additional details on the pretreatment of electrodes and surgical procedure. The electrode was inserted into the cortex in multiple small insertion steps timed about one minute apart to allow the tissue around the electrode time to decompress after each step. In each insertion step, the electrode was driven down 50μm at a rate of 10μm/sec. The signals picked up by all 16 channels were monitored throughout the insertion to confirm each of the 16 channels along the shaft of the electrode had entered the parenchyma. The electrode was inserted to a depth of approximately 1 mm so that the contact sites of the electrode were present in cortical layers I-VI [53]. To minimize variability, the same surgeon performed all implantation surgeries.

For surgical implantation, after a midline incision, skin flaps were cut and clipped away from the surgical area to expose skull. Three holes were drilled in the skull using a 0.45 mm size bit (Stoelting Co.) with adequate breaks in the drilling pulses to prevent overheating of the skull; the electrode hole was created in the skull over the motor region of the brain (1.5 mm lateral and 0.5 mm anterior or posterior to bregma) [54]. The other two craniotomies were for the ground and reference wires in the contralateral hemisphere to the electrode hole (1.5 mm lateral to midline and 1 mm both rostral and caudal to bregma). The electrode was secured to the stereotaxic micromanipulator (Kopf, Model 1760) and lowered down close enough to the skull to insert the ground and reference which were stabilized with silicone elastomer (Kwik-Sil, World Precision Instruments) and self-curing dental acrylic (Stoelting Co.). Epinephrine (1:1000) was then topically applied to the remaining craniotomy for five minutes to constrict the brain vasculature before insertion of the electrode [55]. Following the electrode implantation, silicone elastomer (Kwik-Sil, World Precision Instruments) was used to seal the craniotomy and self-curing dental acrylic (Stoelting Co.) was subsequently added to secure the electrode connector forming a sturdy headcap.

5.6 Neural electrophysiology

Starting one day post-surgery, awake neural recordings, at least 3 minutes in duration, were carried out at least twice a week as described in Hermann *et al.* Details on signal processing can be found in SI, Methods, Section 2.5. Max SNR (an average of the max SNR of single-units for each channel), max amplitude (an average of the max amplitude of single units for each channel), background noise amplitude (an average across all eight channels), number of single units detected per channel, and percent of channels detecting single units were used to quantify IME recording performance. Weekly mean ± standard error of mean were reported for analysis. Neural recording data was statistically evaluated by fitting a mixed effect linear model using Minitab software to each metric used to quantify IME recording performance. Time was discretized into the first twelve weeks and the last four weeks to determine if the quality of neural recording data was different per group during what has been classified as the chronic modified state (CMS) of the effects of IME implantation (after 12 weeks post implantation) [31]. Epoch and group (WT, $Cd14^{-/-}$, Bd$Cd14^{-/-}$, and Mg$Cd14^{-/-}$) were fixed factors and subject (experimental animal) was nested within group as a random effect. The interaction between group and epoch was also added to the mixed effect model. Analysis of variance (ANOVA) was used to determine whether each factor effect or factor interaction effect was statistically significant for both mixed effect models. Significance was considered as $p < 0.05$ unless otherwise noted.

5.7 Signal Processing

Neural data was sampled at 24,414 Hz and bandpass filtered (300-3,000 Hz). The signal was then processed using a common average reference. A custom made MATLAB script was used to remove movement artifact and perform offline spike sorting [56]. Spikes were defined using a negative threshold of 3.5 the standard deviation (SD) of background noise. This background noise is defined by the median (abs(raw voltage))/0.6745[56]. The spike window was defined as 0.49 ms before and 0.98 ms after the threshold crossing event [56]. For signal-to-noise ratio definition, noise was defined at 2 SD of background noise. A previously published unsupervised clustering algorithm was used to cluster spikes into single neuronal units using a minimum cluster size of 20 spikes [56]. Neural units with an SNR > 3 were included in analysis. Furthermore, only the consecutive 8 of 16 channels thought to be in Layer V and VI of the motor cortex were analyzed to coincide with layers targeted for histology and to exclude channels located in cell-poor layers where little or no spiking activity was expected. Electrode placement was calculated based on the depth of insertion and confirmed by the consecutive channels with the most activity over the 16 week study. Since our target layers (V VI) also contain the largest pyramidal cell somas (Fig S4), contacts in those layers should, on average, detect some of the largest amplitude spike waveforms compared to other layers. We confirmed that the distribution of maximum spike amplitudes averaged across animals and time points peaked in the center of the best-consecutive-8 range when each animal's best-consecutive-8 channels used for analysis were aligned.

The key metrics of ‘percentage of working channels’ detecting units and ‘number of units per working channel’ were calculated from each animal's set of best consecutive 8 channels. On the rare occasion where a given channel within the best consecutive 8 was clearly defective (e.g. noise floor an order of magnitude higher than the rest), then that channel would be eliminated from the analysis and metrics would be calculated based on the remaining 7 channels. However, if a given contact within the best consecutive 8 appeared to be intact but detected no units over the course of the study, that channel would be included in the above metrics.

5.8 Immunohistochemistry

Tissue collection—Mice were anesthetized with an intraperitoneal injection of Ketamine/Xylazine cocktail (100 mg/ml Ketamine HCl, 20 mg/ml Xylazine HCl). Mice were then; transcardially perfused with phosphate buffered saline (PBS) until clear of blood, and then 4% paraformaldehyde (PFA) to fix the tissue. Following perfusion, the mouse heads were post-fixed for an additional two days in 4% PFA at 4 °C. After complete fixation, brains were then extracted and equilibrated in 30% sucrose. Microelectrodes were removed, and brains were then cryopreserved in optimal cutting temperature compound (OCT) (Tissue-Tek). Horizontal tissue sections (16 μm thick) were collected and mounted onto glass slides where they were stored at -80 °C.

Immunohistochemistry (IHC) was utilized to assess neuroinflammation and neuronal density in the brain tissue slices, in the area adjacent the implanted IME (SI, Methods). Only tissue slices which include Layer V and VI of the motor cortex, as estimated by depth, were

included for histological assessment [53]. Antibodies used are detailed in SI, Table S2. Analysis of images is described in SI, Methods.

Imaging and quantitative analysis—Image analysis was performed according to previously established protocols [52]. All images were acquired using a Carl Zeiss AxioObserver.Z1 (Zeiss Inc) inverted epifluorescence microscope and a 10× objective. Fluorescent markers on single optical sections were imaged using an AxioCam MRm monochrome camera with fixed exposure times for each marker. All primary and secondary antibodies were previously tested in house to confirm the lack undesirable cross reactivity, prior to use in this study.

Quantification of fluorescence intensity—Raw images of fluorescent markers were analyzed using SECOND, a custom-written MATLAB program previously used [57]. Briefly, the user manually defined the implant hole and imperfections in the brain slice to eliminate from the quantification. Then, the MATLAB program measured the fluorescent intensity of the selected markers in concentric rings at fixed distances from the tissue-electrode interface as a function of distance from the implant. Raw fluorescent intensities of each slice were then normalized to background signal, defined as 600-650 μm of the same slice. To allow for statistical comparisons between conditions, the area under the curve was calculated from the intensity profile for each image. The following data is reported at normalized fluorescent intensity as a function of distance from the tissue-electrode interface. Mean ± standard error of mean were reported for analysis for each 50 μm bin.

Quantification of neuronal densities—Neuronal densities at the interface were determined using AfterNeuN custom-written MATLAB programs [57]. Briefly, the electrode implant region and neuronal cell bodies were defined by the researcher. Using this input, the program then calculated the density of neurons at fixed radial distances from the electrode interface. Neuronal densities at uniform binned distances (50 μm bins) were then normalized to background counts from the same brain tissue slice 500-550 μm away from the interface. Mean ± standard error of mean were reported for analysis for each 50 μm bin.

Immunohistochemistry statistical analysis—To reconcile cortical depth dependencies in brain tissue slices for immunohistochemical markers, measurements from all brain tissue slices for a given animal were first averaged together (4-6 brain slices per animal). Then, comparisons across conditions were performed using independent animal averages. All statistical analyses assessing immunohistochemical results were performed using a general linear model with ANOVA using Minitab software with group and binned distance interval as factors. Pair-wise comparisons using a post-hoc Tukey test with Bonferroni correction were conducted within each ANOVA. Significance was considered as $p < 0.05$.

Supplementary Material

Refer to Web version on PubMed Central for supplementary material.

Acknowledgments

This work was supported in part by the Department of Biomedical Engineering and Case School of Engineering at Case Western Reserve University through laboratory start-up funds, the National Institute of Health, National Institute of Neurological Disorders and Stroke, (Grant # 1R01NS082404-01A1), the NIH Neuroengineering Training Grant 5T- 32EB004314-16. Additional support was provided by the Presidential Early Career Award for Scientists and Engineers (PECASE, JR. Capadona) and by Merit Review Award B1495-R from the United States (US) Department of Veterans Affairs Rehabilitation Research and Development Service. This research was supported by the Tissue Resources Shared Resource of the Case Comprehensive Cancer Center (P30CA043703). The authors would like to thank Dr. Andrew Shoffstall for his help with SEM. None of the funding sources aided in collection, analysis and interpretation of the data, in writing of the manuscript, or in the decision to submit the manuscript for publication. The authors have no conflict of interest related to this work to disclose. The contents do not represent the views of the U.S. Department of Veterans Affairs or the United States Government.

References

1. Ajiboye AB, Willett FR, Young DR, Memberg WD, Murphy BA, Miller JP, Walter BL, Sweet JA, Hoyen HA, Keith MW. Restoration of reaching and grasping movements through brain-controlled muscle stimulation in a person with tetraplegia: a proof-of-concept demonstration. The Lancet. 2017; 389(10081):1821–1830.
2. Schwartz AB. Cortical neural prosthetics. Annu Rev Neurosci. 2004; 27:487–507. [PubMed: 15217341]
3. Liu X, McCreery DB, Bullara LA, Agnew WF. Evaluation of the stability of intracortical microelectrode arrays. IEEE transactions on neural systems and rehabilitation engineering: a publication of the IEEE Engineering in Medicine and Biology Society. 2006; 14(1):91–100.
4. Barrese JC, Rao N, Paroo K, Triebwasser C, Vargas-Irwin C, Franquemont L, Donoghue JP. Failure mode analysis of silicon-based intracortical microelectrode arrays in non-human primates. J Neural Eng. 2013; 10(6):066014. [PubMed: 24216311]
5. Rennaker RL, Miller J, Tang H, Wilson DA. Minocycline increases quality and longevity of chronic neural recordings. J Neural Eng. 2007; 4(2):L1–5. [PubMed: 17409469]
6. Polikov VS, Tresco PA, Reichert WM. Response of brain tissue to chronically implanted neural electrodes. J Neurosci Methods. 2005; 148(1):1–18. [PubMed: 16198003]
7. Jorfi M, Skousen JL, Weder C, Capadona JR. Progress towards biocompatible intracortical microelectrodes for neural interfacing applications. Journal of Neural Engineering. 2015; 12(1): 011001. [PubMed: 25460808]
8. Saxena T, Karumbaiah L, Gaupp EA, Patkar R, Patil K, Betancur M, Stanley GB, Bellamkonda RV. The impact of chronic blood–brain barrier breach on intracortical electrode function. Biomaterials. 2013; 34(20):4703–4713. [PubMed: 23562053]
9. Kozai TDY, Li X, Bodily LM, Caparosa EM, Zenonos GA, Carlisle DL, Friedlander RM, Cui XT. Effects of caspase-1 knockout on chronic neural recording quality and longevity: Insight into cellular and molecular mechanisms of the reactive tissue response. Biomaterials. 2014; 35(36): 9620–9634. [PubMed: 25176060]
10. Hermann JK, Ravikumar M, Shoffstall A, Ereifej E, Kovach K, Chang J, Soffer A, Wong C, Srivastava V, Smith P, Protasiewicz G, Jiang J, Selkirk SM, Miller RH, Sidik S, Ziats NP, Taylor DM, Capadona JR. Inhibition of the Cluster of Differentiation 14 Innate Immunity Pathway with IAXO-101 Improves Chronic Microelectrode Performance. Journal of neural engineering ((Under Revision)).
11. Hermann JK, Ravikumar M, Shoffstall A, Ereifej E, Kovach K, et al. Inhibition of the cluster of differentiation 14 innate immunity pathway with IAXO-101 improves chronic microelectrode performance. Journal of Neural Engineering. 2017
12. Ravikumar M, Sunil S, Black J, Barkauskas D, Haung AY, Miller RH, Selkirk SM, Capadona JR. The Roles of Blood-derived Macrophages and Resident Microglia in the Neuroinflammatory Response to Implanted Intracortical Microelectrodes. Biomaterials. 2014; S0142-9612(35):8049–8064.

13. Kim S, Kim SY, Pribis JP, Lotze M, Mollen KP, Shapiro R, Loughran P, Scott MJ, Billiar TR. Signaling of high mobility group box 1 (HMGB1) through toll-like receptor 4 in macrophages requires CD14. Mol Med. 2013; 19:88–98. [PubMed: 23508573]
14. Potter KA, Jorfi M, Householder KT, Foster EJ, Weder C, Capadona JR. Curcumin-releasing mechanically adaptive intracortical implants improve the proximal neuronal density and blood-brain barrier stability. Acta Biomater. 2014; 10(5):2209–22. [PubMed: 24468582]
15. Scaffidi P, Misteli T, Bianchi ME. Release of chromatin protein HMGB1 by necrotic cells triggers inflammation. Nature. 2002; 418(6894):191–5. [PubMed: 12110890]
16. Haziot A, Chen S, Ferrero E, Low M, Silber R, Goyert S. The monocyte differentiation antigen, CD14, is anchored to the cell membrane by a phosphatidylinositol linkage. The Journal of Immunology. 1988; 141(2):547–552. [PubMed: 3385210]
17. Beschorner R, Nguyen TD, Gözalan F, Pedal I, Mattern R, Schluesener HJ, Meyermann R, Schwab JM. CD14 expression by activated parenchymal microglia/macrophages and infiltrating monocytes following human traumatic brain injury. Acta neuropathologica. 2002; 103(6):541–549. [PubMed: 12012085]
18. Yang RB, Mark MR, Gurney AL, Godowski PJ. Signaling events induced by lipopolysaccharide-activated toll-like receptor 2. The Journal of Immunology. 1999; 163(2):639–643. [PubMed: 10395652]
19. Okamura Y, Watari M, Jerud ES, Young DW, Ishizaka ST, Rose J, Chow JC, Strauss JF. The extra domain A of fibronectin activates Toll-like receptor 4. Journal of Biological Chemistry. 2001; 276(13):10229–10233. [PubMed: 11150311]
20. Smiley ST, King JA, Hancock WW. Fibrinogen stimulates macrophage chemokine secretion through toll-like receptor 4. The Journal of Immunology. 2001; 167(5):2887–2894. [PubMed: 11509636]
21. Beg AA. Endogenous ligands of Toll-like receptors: implications for regulating inflammatory and immune responses. Trends in Immunology. 2002; 23(11):509–512. [PubMed: 12401394]
22. Li M, Carpio DF, Zheng Y, Bruzzo P, Singh V, Ouaaz F, Medzhitov RM, Beg AA. An essential role of the NF-κB/Toll-like receptor pathway in induction of inflammatory and tissue-repair gene expression by necrotic cells. The Journal of Immunology. 2001; 166(12):7128–7135. [PubMed: 11390458]
23. Asea A, Kraeft SK, Kurt-Jones EA, Stevenson MA, Chen LB, Finberg RW, Koo GC, Calderwood SK. HSP70 stimulates cytokine production through a CD14-dependant pathway, demonstrating its dual role as a chaperone and cytokine. Nature medicine. 2000; 6(4):435–442.
24. He Z, Riva M, Bjork P, Sward K, Morgelin M, Leanderson T, Ivars F. CD14 Is a Co-Receptor for TLR4 in the S100A9-Induced Pro-Inflammatory Response in Monocytes. PLoS One. 2016; 11(5):e0156377. [PubMed: 27228163]
25. Chun KH, Seong SY. CD14 but not MD2 transmit signals from DAMP. Int Immunopharmacol. 2010; 10(1):98–106. [PubMed: 19840871]
26. Devitt A, Moffatt OD, Raykundalia C, Capra JD. Human CD14 mediates recognition and phagocytosis of apoptotic cells. Nature. 1998; 392(6675):505. [PubMed: 9548256]
27. Pineau I, Lacroix S. Endogenous signals initiating inflammation in the injured nervous system. Glia. 2009; 57(4):351–61. [PubMed: 18803306]
28. Kielian T. Toll-like receptors in central nervous system glial inflammation and homeostasis. Journal of Neuroscience Research. 2006; 83(5):711–730. [PubMed: 16541438]
29. Segura M, Vadeboncoeur N, Gottschalk M. CD14-dependent and-independent cytokine and chemokine production by human THP-1 monocytes stimulated by Streptococcus suis capsular type 2. Clinical & Experimental Immunology. 2002; 127(2):243–254. [PubMed: 11876746]
30. Reed-Geaghan EG, Savage JC, Hise AG, Landreth GE. CD14 and toll-like receptors 2 and 4 are required for fibrillar A{beta}-stimulated microglial activation. The Journal of neuroscience: the official journal of the Society for Neuroscience. 2009; 29(38):11982–92. [PubMed: 19776284]
31. Prodanov D, Delbeke J. Mechanical and Biological Interactions of Implants with the Brain and Their Impact on Implant Design. Front Neurosci. 2016; 10:11. [PubMed: 26903786]

32. Graeber MB, Streit WJ, Kiefer R, Schoen SW, Kreutzberg GW. New expression of myelomonocytic antigens by microglia and perivascular cells following lethal motor neuron injury. Journal of neuroimmunology. 1990; 27(2):121–132. [PubMed: 2332482]
33. Anderson JM. Biological responses to materials. Annu Rev Mater Res. 2001; 31:81–110.
34. Nolta NF, Christensen MB, Crane PD, Skousen JL, Tresco PA. BBB leakage, astrogliosis, and tissue loss correlate with silicon microelectrode array recording performance. Biomaterials. 2015; 53:753–762. [PubMed: 25890770]
35. Selvakumaran J, Keddie JL, Ewins DJ, Hughes MP. Protein adsorption on materials for recording sites on implantable microelectrodes. Journal of Materials Science: Materials in Medicine. 2008; 19(1):143–151. [PubMed: 17587151]
36. Biran R, Martin D, Tresco P. Neuronal cell loss accompanies the brain tissue response to chronically implanted silicon microelectrode arrays. Exp Neurol. 2005; 195(1):115–126. [PubMed: 16045910]
37. Landis DMD. The Early Reactions of Nonneuronal Cells to Brain Injury. Annu Rev Neurosci. 1994; 17:133–151. [PubMed: 8210172]
38. Buzsáki G. Large-scale recording of neuronal ensembles. Nat Neurosci. 2004; 7(5):446–451. [PubMed: 15114356]
39. Potter KA, Buck AC, Self WK, Capadona JR. Stab injury and device implantation within the brain results in inversely multiphasic neuroinflammatory and neurodegenerative responses. J Neural Eng. 2012; 9(4):046020. [PubMed: 22832283]
40. McConnell GC, Rees HD, Levey AI, Gutekunst CA, Gross RE, Bellamkonda RV. Implanted neural electrodes cause chronic, local inflammation that is correlated with local neurodegeneration. J Neural Eng. 2009; 6(5):056003. [PubMed: 19700815]
41. Lawrence T. The nuclear factor NF-κB pathway in inflammation. Cold Spring Harbor perspectives in biology. 2009; 1(6):a001651. [PubMed: 20457564]
42. Ajami B, Bennett JL, Krieger C, McNagny KM, Rossi FMV. Infiltrating monocytes trigger EAE progression, but do not contribute to the resident microglia pool. Nature Neuroscience. 2011; 14(9):1142–1149. [PubMed: 21804537]
43. Evans TA, Barkauskas DS, Myers JT, Hare EG, You JQ, Ransohoff RM, Huang AY, Silver J. High-resolution intravital imaging reveals that blood-derived macrophages but not resident microglia facilitate secondary axonal dieback in traumatic spinal cord injury. Exp Neurol. 2014; 254C:109–120.
44. Fumagalli S, Perego C, Pischiutta F, Zanier ER, De Simoni MG. The ischemic environment drives microglia and macrophage function. Frontiers in neurology. 2015; 6
45. Woolley AJ, Desai HA, Otto KJ. Chronic intracortical microelectrode arrays induce non-uniform, depth-related tissue responses. Journal of neural engineering. 2013; 10(2):026007. [PubMed: 23428842]
46. Kozai T, Marzullo T, Hooi F, Langhals N, Majewska A, Brown E, Kipke D. Reduction of neurovascular damage resulting from microelectrode insertion into the cerebral cortex using in vivo two-photon mapping. Journal of Neural Engineering. 2010; 7(4):046011. [PubMed: 20644246]
47. Potter KA, Simon JS, Velagapudi B, Capadona JR. Reduction of autofluorescence at the microelectrode-cortical tissue interface improves antibody detection. J Neurosci Methods. 2012; 203(1):96–105. [PubMed: 21978484]
48. Kim BJ, Kuo JT, Hara SA, Lee CD, Yu L, Gutierrez C, Hoang T, Pikov V, Meng E. 3D Parylene sheath neural probe for chronic recordings. Journal of Neural Engineering. 2013; 10(4):045002. [PubMed: 23723130]
49. McCreery D, Cogan S, Kane S, Pikov V. Correlations between histology and neuronal activity recorded by microelectrodes implanted chronically in the cerebral cortex. J Neural Eng. 2016; 13:036012. [PubMed: 27108712]
50. Takmakov P, Ruda K, Phillips KS, Isayeva IS, Krauthamer V, Welle CG. Rapid evaluation of the durability of cortical neural implants using accelerated aging with reactive oxygen species. Journal of Neural Engineering. 2015; 12(2):026003. [PubMed: 25627426]

51. Potter-Baker KA, Capadona JR. Reducing the “Stress”: Antioxidative Therapeutic and Material Approaches May Prevent Intracortical Microelectrode Failure. ACS Macro Letters. 2015:275–279.

52. Nguyen JK, Park DJ, Skousen JL, Hess-Dunning AE, Tyler DJ, Rowan SJ, Weder C, Capadona JR. Mechanically-compliant intracortical implants reduce the neuroinflammatory response. J Neural Eng. 2014; 11(5):056014. [PubMed: 25125443]

53. Oswald MJ, Tantirigama ML, Sonntag I, Hughes SM, Empson RM. Diversity of layer 5 projection neurons in the mouse motor cortex. Front Cell Neurosci. 2013; 7:174. [PubMed: 24137110]

54. Tennant KA, Adkins DL, Donlan NA, Asay AL, Thomas N, Kleim JA, Jones TA. The organization of the forelimb representation of the C57BL/6 mouse motor cortex as defined by intracortical microstimulation and cytoarchitecture. Cerebral cortex. 2011; 21(4):865–876. [PubMed: 20739477]

55. Richter A, Xie Y, Schumacher A, Löffler S, Kirch RD, Al-Hasani J, Rapoport DH, Kruse C, Moser A, Tronnier V. A simple implantation method for flexible, multisite microelectrodes into rat brains. Frontiers in neuroengineering. 2013; 6

56. Quiroga RQ, Nadasdy Z, Ben-Shaul Y. Unsupervised spike detection and sorting with wavelets and superparamagnetic clustering. Neural computation. 2004; 16(8):1661–87. [PubMed: 15228749]

57. Goss-Varley M, Dona KR, McMahon JA, Shoffstall AJ, Ereifej ES, Lindner SC, Capadona JR. Microelectrode implantation in motor cortex causes fine motor deficit: Implications on potential considerations to Brain Computer Interfacing and Human Augmentation. Scientific Reports In Press. 2017

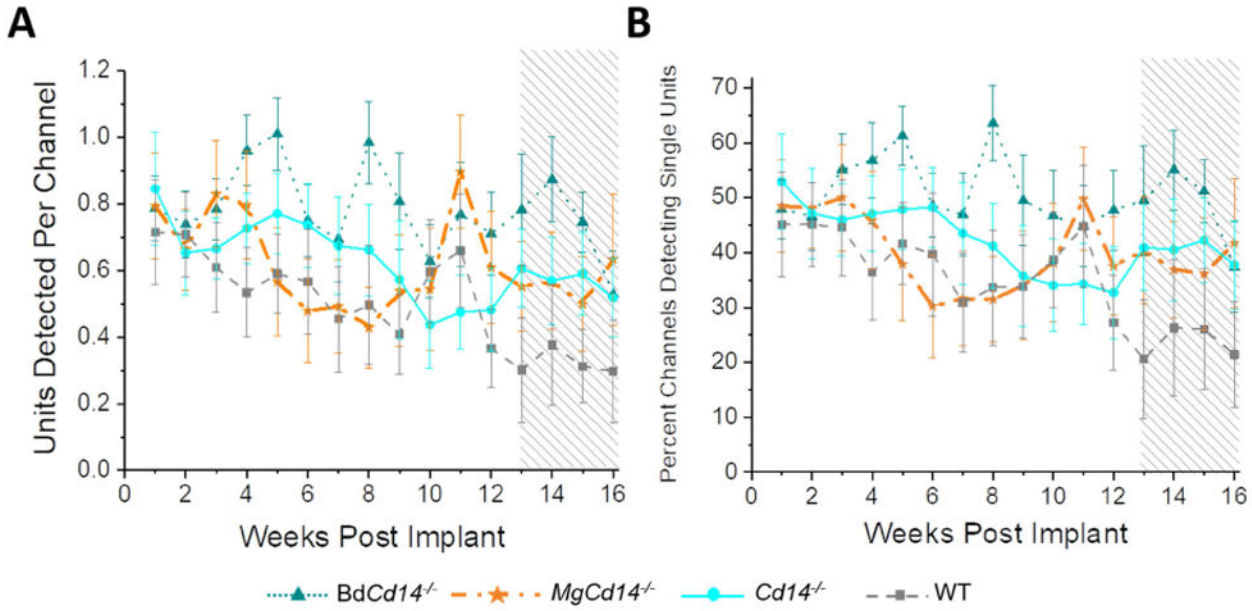

Figure 1. Recording performance for all four animal models

Number of single units detected per working channel (A) and percentage of working channels detecting single units (B). Shaded region on the plots represents the CMS time course.

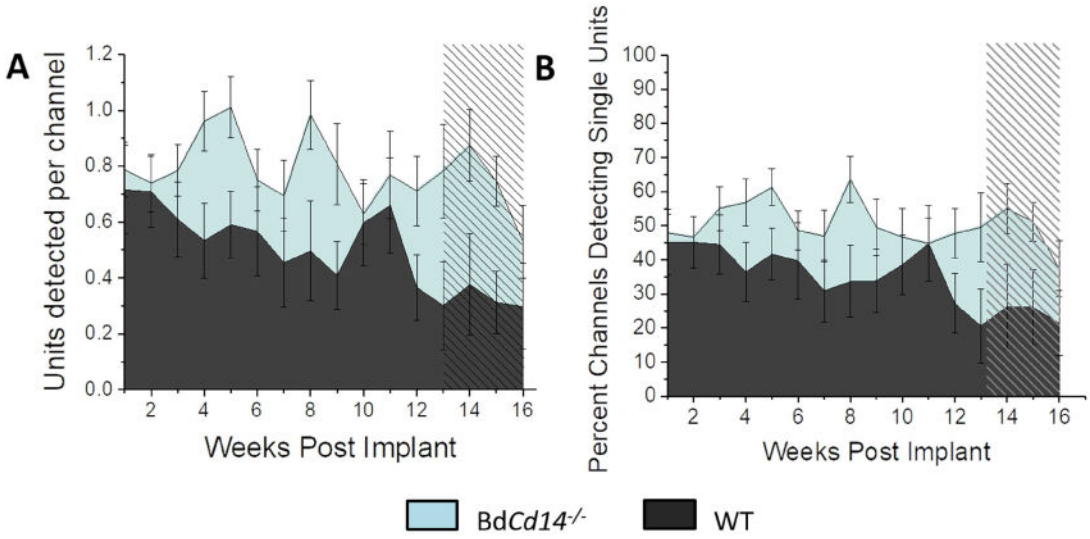

Figure 2. Recording performance for removing BdCD14 versus WT

Number of single units detected per working channel (A) and percentage of working channels detecting single units (B). Shaded region on the plots represents the CMS time course.

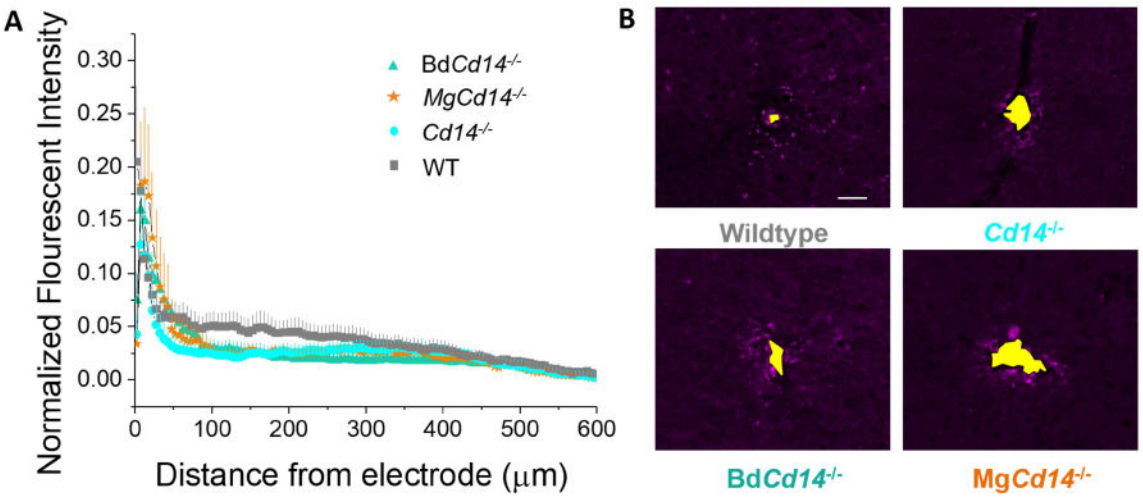

Figure 3. Immunohistochemical evaluation of inflammatory activated microglia and macrophages

(A) Microglial and macrophage activation evaluated as CD68 expression with respect to distance from the explanted microelectrode hole (μm). No significant differences were observed among experimental groups. (B) Representative images from tissue derived from ~ 480 - 800 μm deep from surface of brain. Yellow area represents hole left by explanted probe. Scale bar: 50 μm.

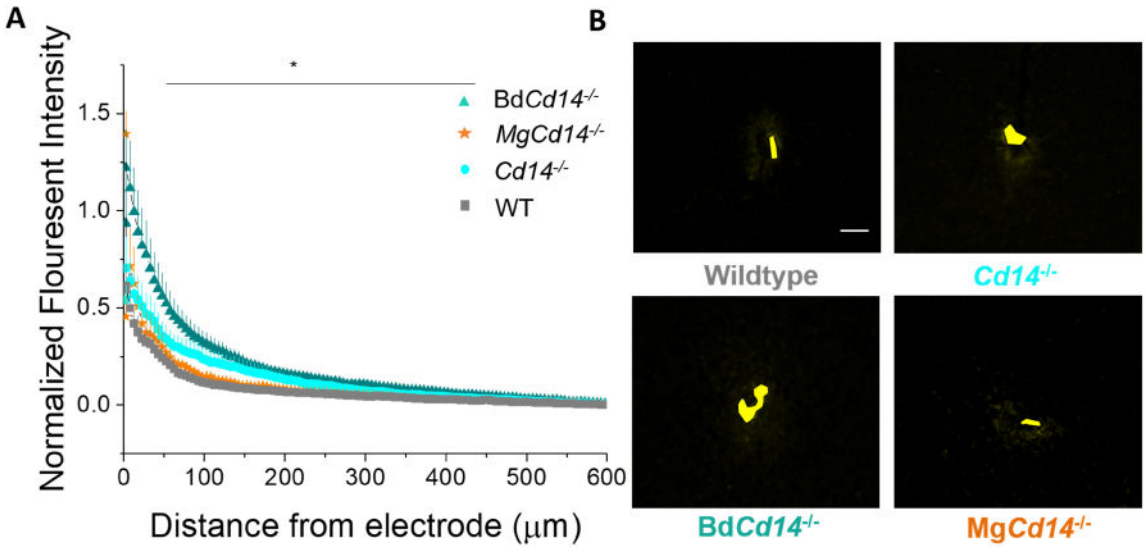

Figure 4. Immunohistochemical evaluation of blood brain barrier permeability

(A) Blood brain barrier permeability evaluated as IgG expression with respect to distance from the explanted microelectrode hole (μm). Significant differences between wildtype and Bd*Cd14*$^{-/-}$ were observed from 50-450 μm away from electrode-tissue interface, * $p<0.05$). (B) Representative images from tissue derived from ~380 - 830 μm deep from surface of brain. Yellow area represents hole left by explanted probe. Scale bar: 50 μm

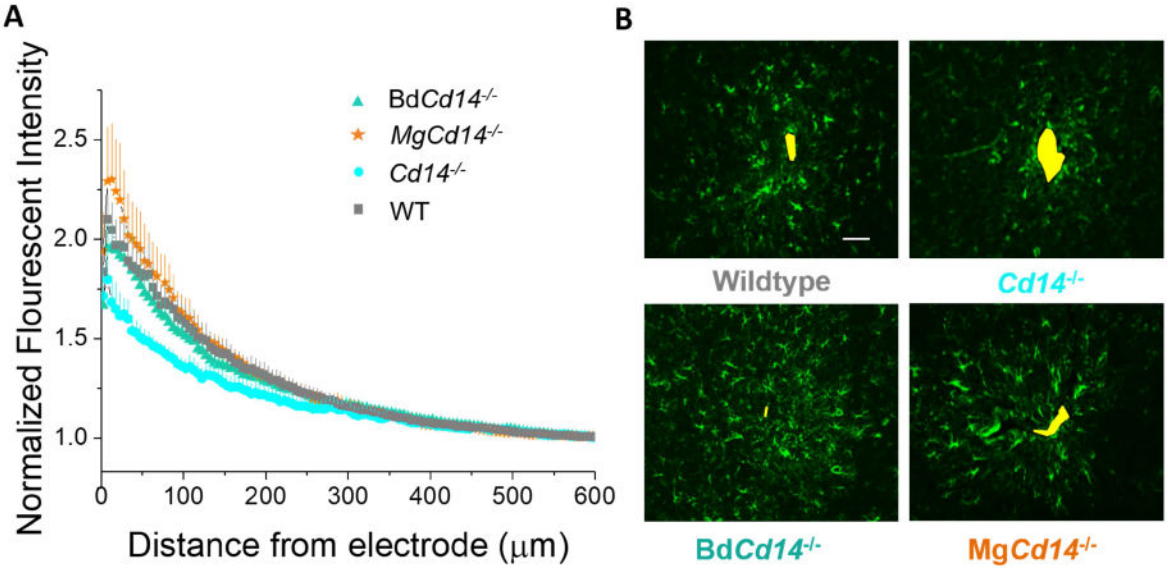

Figure 5. Immunohistochemical evaluation of astrocyte encapsulation

(A) Astrocyte encapsulation evaluated as GFAP expression with respect to distance from the explanted microelectrode hole (μm). No significant differences were observed among experimental groups. (B) Representative images from tissue derived from ~ 380 - 940 μm deep from surface of brain. Yellow area represents hole left by explanted probe. Scale bar: 50 μm

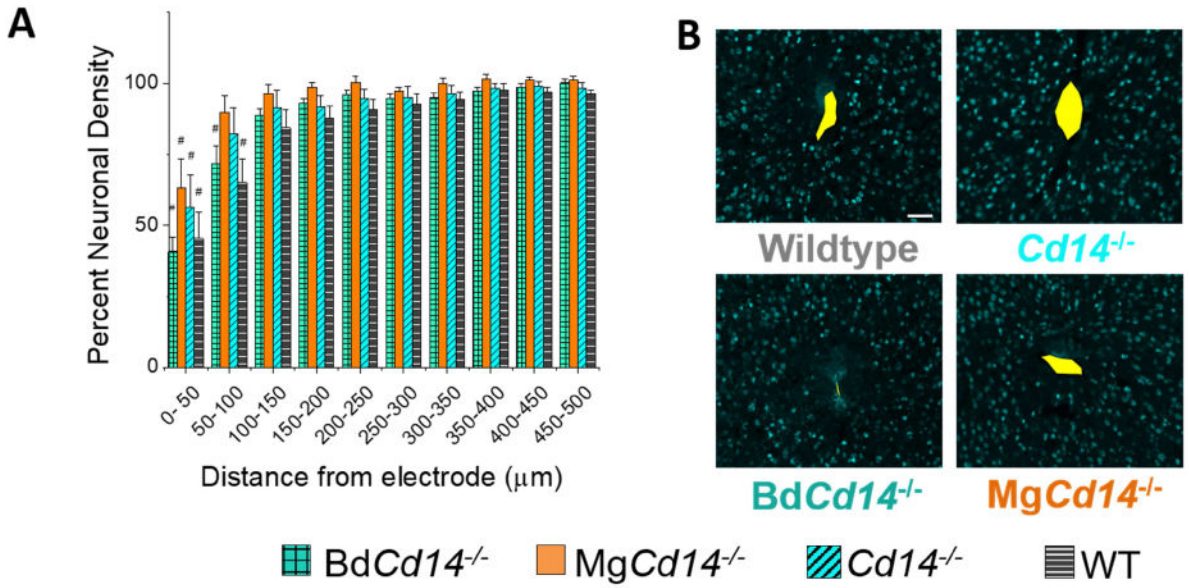

Figure 6. Immunohistochemical evaluation of neuronal density

(A) Neuronal density evaluated as NeuN+ counts with respect to distance from the explanted microelectrode hole (μm). No significant differences were observed among experimental groups. Neuronal density is significantly different from background Mg*Cd14*$^{-/-}$ and wildtype between 0 and 50 μm from the microelectrode hole, and *Cd14*$^{-/-}$ and Bd*Cd14*$^{-/-}$ between 0 and 100 μm from the microelectrode hole, # $p<0.05$. (B) Representative images from tissue acquired from ~625-825 μm deep from surface of brain. Yellow area represents hole left by explanted probe. Scale bar: 50 μm

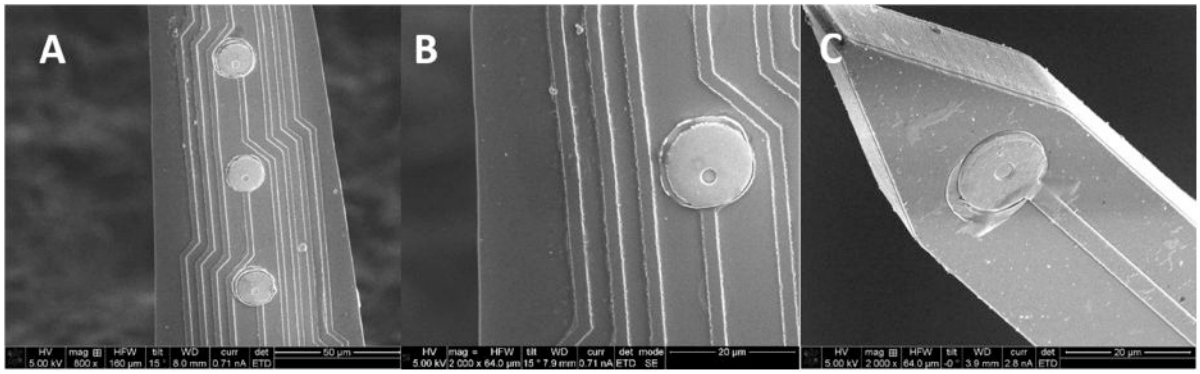

Figure 7. Representative SEM images of post-explant and non-implanted laminar, silicon IMEs

(A) Probe explanted after 16 week study (800× magnification). (B) Probe explanted after 16 week study (2000× magnification). (C) Non-implanted probe (2000× magnification).

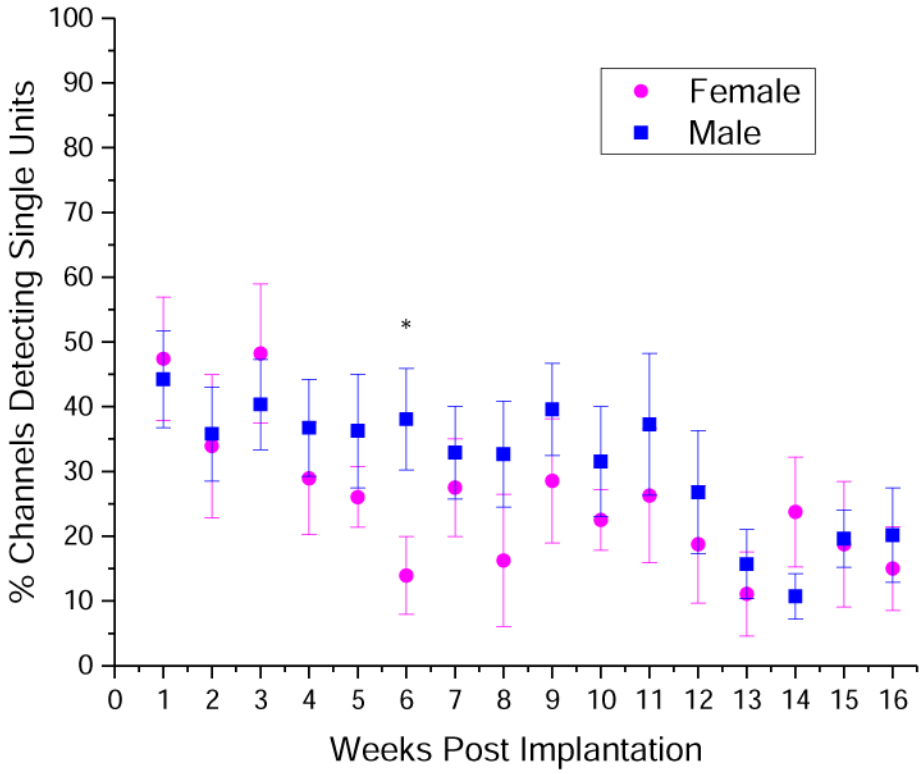

Figure 8. Sex as a Biological Variable

Both male (n=11) and female (n=8) mice were implanted with control NeuroNexus Single shank, 16 channel Michigan style electrodes in primary motor cortex. Over a 16 week trial, only one time point showed a significant difference in the percentage of channels detecting single units. * $p<0.05$.

Table 1

Statistical summary for the recording performance of laminar, silicon IME comparing all experimental groups (top) and WT versus Bd*Cd14*$^{-/-}$ (bottom). Numbers displayed are p values and shaded boxes are significant.

Comparison	Units per Channel	Percentage of Channels Detecting Single Units
	Comparing all four experimental groups	
Group	0.192	0.334
Dynamic vs CMS	0.03	0.027
Group * Dynamic vs CMS	0.061	0.009
	Comparing WT to Bd*Cd14*$^{-/-}$	
Group	0.016	0.045
Dynamic vs CMS	0.008	0.004
Group * Dynamic vs CMS	0.080	0.087